

Simulation Standard

Connecting TCAD To Tapeout

A Journal for Process and Device Engineers

Electrostatic Effect of Localized Charge in Dual Bit Memory Cells with Discrete Traps

L. Perniola(1, 2,*), S. Bernardini(3), G. Iannaccone(1,6), B. De Salvo (4), G. Ghibaudo (2), P. Masson(3), C. Gerardi(5)

(1)Dipartimento di Ingegneria dell'Informazione, Università degli Studi di Pisa, Via Caruso, 56122 Pisa, Italy, *perniola@enserg.fr

(2)IMEP-CNRS/INPG, Avenue de Martyrs 32, 38016 Grenoble, France

(3) L2MP-Polytech – IMT Technopôle de Château Gombert, 13451 Marseille Cedex 20 France

(4)CEA-LETI, Avenue de Martyrs 16, 38054 Grenoble, France (5)STMicroelectronics, Catania, Italy (6)IEIT-CNR, Via Caruso, 56122 Pisa, Italy.

The following article, presented at ESSDERC 2004 conference, illustrates the capability of *ATLAS* in the validation and the comprehension of complex effects of new promising devices like non-volatile discrete traps memory devices.

Abstract

In this paper the electrostatic impact of Channel Hot Electron (CHE) injection in discrete-trap memories is quantitatively addressed. The dual bit behavior of the transfer characteristic during forward and reverse read of a written cell is thoroughly analysed with the help of an analytical model. Such model allows, for the first time, to estimate the effective charged portion of the discrete storage layer, L_{eff} , and the quantity of electrons, Q , injected in the trapping sites from the experimental parameters of the I_d - V_g characteristics, the reverse-forward threshold voltage shift ΔV_{RFE} , and the total threshold voltage shift ΔV_{tot} . The viability of this model is confirmed with tests performed on nanocrystal memories, under different bias conditions. These results are confirmed with the help of a 2D drift-diffusion commercial code (*ATLAS-SILVACO*).

1. Introduction

Channel Hot Electron injection is widely used as a standard writing method for non-volatile discrete-trap memory products [1]-[2]. It provides the opportunity to localise the charges injected in a small region of the trapping medium, and two-bit operation is achieved through multilevel storage [3]. The basic principle on which two-bit operation resides, is common to NROM memories and nanocrystal memories [4]-[5]. It is possible to trap charges near one junction (drain or source) with a programming stress, and read them in the *reverse* mode, compared to the programming, enhancing the electrostatic effect of these charges on the conductivity of the active channel (see Figure 1).

It has been shown in the literature [1]-[3]-[6] that the threshold voltage during the *forward* read, $V_{\text{th-F}}$ is lower

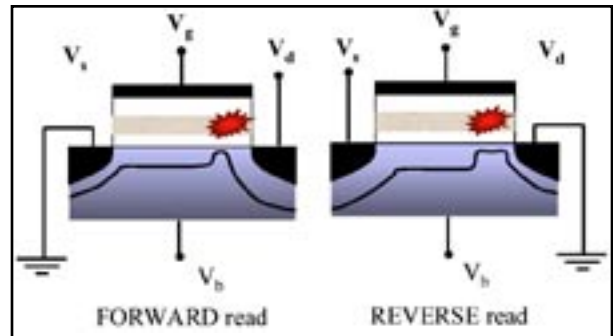


Figure 1. The concept of forward and reverse read after Channel Hot Electron programming, considering a non zero bulk potential. In the figure the depletion width under the charged and uncharged regions is highlighted.

than the threshold voltage during the reverse read, $V_{\text{th-R}}$ when the cell is polarised in the saturation regime.

This is due to the strong two dimensional effects near the charged junction. If the injected charge, near the drain, is completely screened by the high V_{ds} applied in forward read (which induces a long pinchoff region), the I_d - V_g characteristic results very close to the characteristic of the fresh cell. In this case we have a low $V_{\text{th-F}}$. On the other hand, during the reverse read the high V_{ds} applied is not able to screen the effect of electrons and the conductivity of the active channel is lowered by the "bottleneck" near the low-voltage contact. In such a case we have a high $V_{\text{th-R}}$ [2]-[6].

Continued on page 2 ...

INSIDE

A New Efficient Quantum Method:

The Bohm Quantum Potential Model..... 6

Simulating Selective and Non-Selective Epitaxy over Oxide Isolated Regions Using ATHENA 9

Calendar of Events10

Hints, Tips, and Solutions11

With a simple 1D approach (Gradual Channel Approximation) [6] it is not possible to simulate such an asymmetric behavior. In this paper, with the help of a simple quasi 2D analytical approach, we are able to quantify for the first time, both the length of the charged region, L_c , and the number of injected electrons per unit area in the trapping sites, Q , from the two quantities available from experiments, the *total threshold voltage shift*, ΔV_{th-tot} (i.e., the difference between the threshold voltage in the reverse read, V_{th-R} and the threshold voltage of the fresh cell, $V_{th-fresh}$) and the *reverse-forward threshold voltage shift*, ΔV_{RF} (i.e. the difference between V_{th-R} and V_{th-P}).

The viability of the model is tested with 2D numerical simulations of a commercial TCAD code (*ATLAS-SILVACO*).

Main results from the theory are widely tested, under different bias conditions, on nanocrystal memories fabricated by ST-Microelectronics [4]. The influence of the bulk potential, as well as that of the drain-to-source potential, are carefully assessed in this work.

2. Quasi-2D Analytical Model

With a simple 1D approach it is not possible to describe properly the 2D effects near the charged region, which are the first cause of the dual bit behavior. For the first time, to our knowledge, we present an analytical approach, which starts from quasi 2D considerations [7].

The analytical approach describes the behavior of the surface potential Ψ_s along the channel of a MOSFET with non-uniform threshold voltage. The distribution of trapped charge may be in general a complicate function of the spatial coordinates. We assume that the charge distribution along the channel can be described by a step function which represents an "effective" distribution. As a result, we can distinguish two regions: one close to the source with a length L_1 where storage nodes are not charged (uncharged

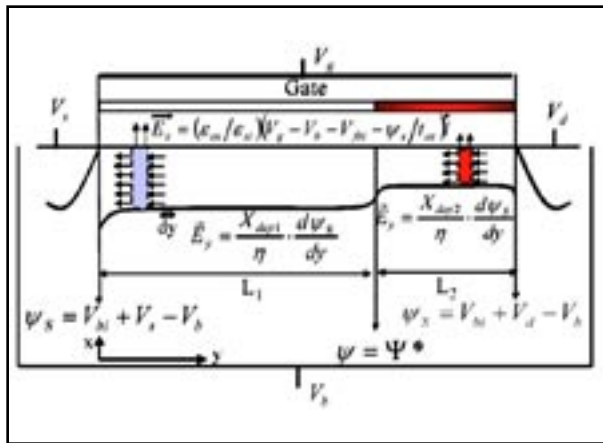


Figure 2. Sketch of the charged and uncharged regions. Equation (2) and (3) come from the Gauss' law applied to the two slices of thickness dy . Boundary conditions are shown (V_{bi} is the built-in potential), considering the presence of a bulk voltage V_b . The potential reference value is the Fermi level of the bulk.

region); and the second one close to the drain with a length L_2 which is uniformly charged by Q electrons per unit area. In Figure 2 it can be seen how the written memory is divided in the two regions. The trapped charge raises the flat band voltage, V_{fb-2} of the charged region L_2 . In particular the flat band voltage difference between the charged and the uncharged region is:

$$\Delta V_{fb} = + \frac{Q \cdot q}{C_2} \quad (1)$$

Where q is the electron charge, C_2 is the top oxide capacitance per unit area.

In the following model, we do not consider charges over the drain junction, but, as already noted by [6], from Figure 3 it appears that they do not influence I_d - V_g characteristics.

The model solves separately, in the two regions, the differential equations (2) and (3). Gauss' law is applied to a transversal slice of thickness dy along y and cross section equal to the average depletion width X_{depi} ($i=1,2$) (see Figure 2), and allows us to write the flux of the electric field through the faces perpendicular to y in terms of the surface potential as $(X_{depi} \ln) d\Psi_s/dy$, where η is a fitting parameter. During the gate voltage sweep, frequently the uncharged region goes in strong inversion, while the charged region is still pinched-off. The presence of both inversion charge Q_{inv} and depletion charge at inversion Q_{depi} are carefully considered in Equation (3):

$$\epsilon_{ox} \frac{X_{depi1}}{\eta} \frac{d^2 \Psi_s}{dy^2} + \epsilon_{ox} \frac{V_g - V_s - V_{bi} - \Psi_s}{t_{ox}} = Q_{depi1} + Q_{inv} \quad (2)$$

$$\epsilon_{ox} \frac{X_{depi2}}{\eta} \frac{d^2 \Psi_s}{dy^2} + \epsilon_{ox} \frac{V_g - V_s - V_{bi} - \Psi_s}{t_{ox}} = qN_{inv}X_{depi2} \quad (3)$$

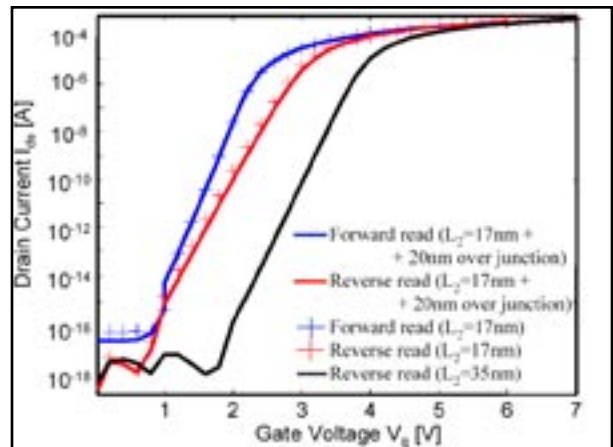


Figure 3. *ATLAS* simulations to assess the influence of charge over drain junction. It is clear that a charged region over the junction of length comparable to L_2 , has negligible effects on channel conductivity.

where ϵ_{si} (ϵ_{ox}) is the silicon (oxide) electric permittivity, V_g the gate voltage, t_{ox} is the equivalent oxide thickness, N_{sub} is the doping level of the bulk. If a bulk voltage, V_b is applied, as sketched in Figure 2, the drain, source and gate potentials must be raised of V_b setting at zero the potential of the bulk. The space charge and the inversion charge have the following expression:

$$Q_{dep} = \sqrt{2\epsilon_{ox}qN_{sub} \cdot (\Psi_{L-i} - V_s)} \quad (4)$$

$$Q_{inv} = \frac{KT}{q} mC_{ox} \ln[1 + \frac{C_{dep}}{mC_{ox}} \exp(\frac{q}{mKT} (V_{gs} - V_{ds,i}) - \frac{qU_{cs}}{KT})] \quad (5)$$

Where $i=1,2$, Ψ_{L-i} is the surface potential in the case the influence of drain and source junctions is completely neglected, U_{cs} is the quasi-Fermi potential referred to the source of the uncharged equivalent transistor.

The solution to Equation (2) is a linear combination of hyperbolic sins:

$$\Psi_{s-1}(y) = (\Psi_{r-1} - \Psi_{l-1}) \frac{\sinh(y/\lambda_s)}{\sinh(L_1/\lambda_s)} + (\Psi_{l-1} - \Psi_{r-1}) \frac{\sinh((y-L_1)/\lambda_s)}{\sinh(L_1/\lambda_s)} \quad (6)$$

where Ψ_{r-1} (Ψ_{l-1}) is the right-hand (left-hand) boundary condition shown in Figure 2. Ψ_{s-1} is referred to the value of the potential in the bulk. The solution to Equation (3) is of similar form of Equation (6).

The parameter $\lambda = \sqrt{\epsilon_{si} t_{ox} X_{depl} / (\epsilon_{ox} \eta)}$ describes the *short channel effects*, as it provides a clue on how strong is the influence of the junction potential on Ψ_s under the gate. The higher the value of λ , the smoother appears the Ψ_s curve along the channel, the weaker is the control effect of the gate on the channel.

From the description of the surface potential, the drain current can be calculated. As in the subthreshold region the current is a *diffusion* dominated process, the following expression can be derived [8]:

$$I_{ds} = \mu_{eff} \frac{W}{L} \sqrt{\frac{\epsilon_{ox} q N_{sub}}{2(\Psi_{smin} + V_s)}} \left(\frac{KT}{q}\right)^2 \left(\frac{n_i}{N_{sub}}\right)^2 e^{-\frac{q(\Psi_{smin} + V_s)}{KT}} \quad (7)$$

where μ_{eff} is the effective mobility of electrons in the channel, KT is the thermal energy, n_i is the intrinsic electron concentration in silicon and Ψ_{smin} is the minimum of the surface potential in the channel.

3. Comparison Between the Analytical Model and ATLAS Results

From Equation (2), the importance of η is apparent.

To determine the proper value of this parameter, we have used the commercial TCAD tool *ATLAS* from SILVACO. We have simulated a class of nanocrystal memories, fabricated from STMicroelectronics. Parameters of the memory cell are $L=0.28 \mu m$, $W=0.16 \mu m$, tunnelling oxide thickness $t_{tun-ox}=5.5 \text{ nm}$, control oxide thickness $t_2=8 \text{ nm}$. The charged nanocrystals have been considered as a uniform charged oxide region, of thickness $t_{ch}=2 \text{ nm}$, sandwiched between the tunnelling oxide and the control gate oxide.

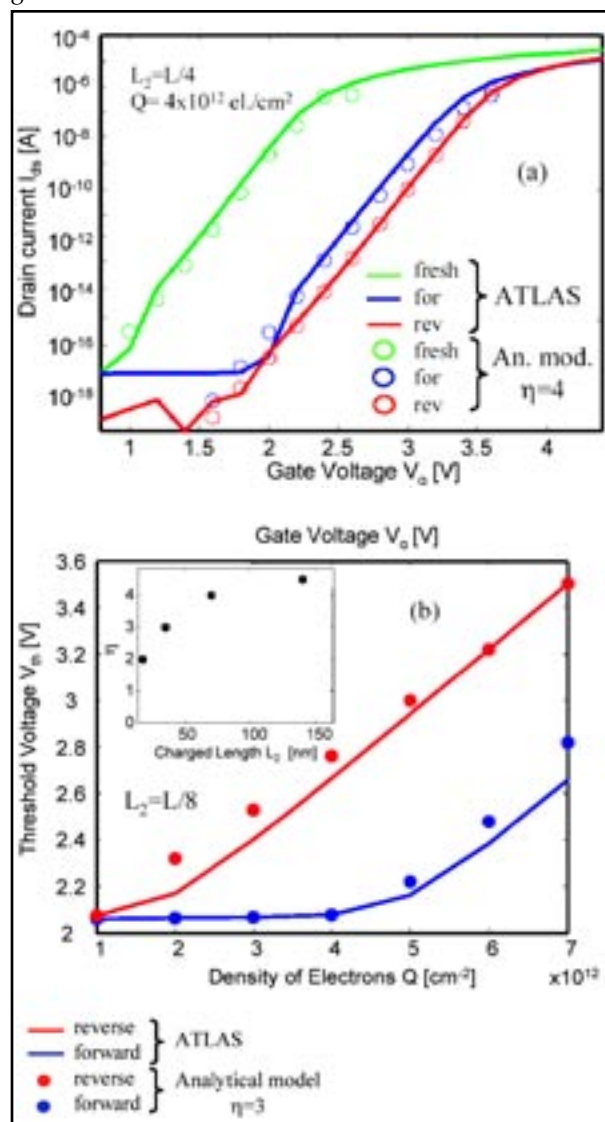


Figure 4 (a) Comparison of the transfer characteristics from *ATLAS* (solid lines) and analytical model (circles) to extract the value of the fitting parameter η . In the case of $L_2=L/4$, the best value is $\eta=4$. (b) Comparison of V_{th} versus Q obtained with *ATLAS* (solid lines) and the analytical model (circles) shows that η is weakly dependent on the density of electrons injected in dots. In the inset of Figure 4(b) the dependence of η on L_2 is provided.

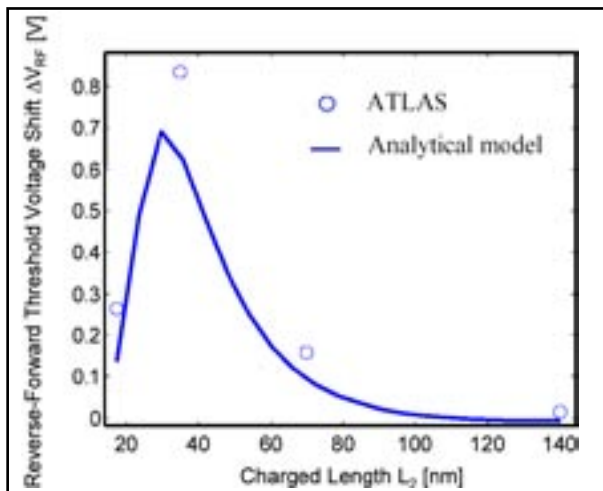


Figure 5. Reverse-forward threshold voltage shift ΔV_{RF} as a function of the charged length L_2 obtained from **ATLAS** (circles) and the analytical model (solid line). Parameters are dot density 10^{12} cm^{-2} , 6 el./dot and η according to the inset of Figure 4(b).

As specified before, we simply assumed that the charge distribution in the oxide is a step function where the charged length can be varied and the density of charge has been chosen to fit different flat band voltages V_{fb} 's.

In Figure 4(a) a sample comparison between **ATLAS** results and the analytical model for $L_2=L/4$ is shown. The parameter η to fit I_d-V_g numerical characteristics has shown a weaker dependence on the density of electrons trapped in dots, Q , than on the charged length L_2 . This property is shown in Figure 4(b), where, provided one value of L_2 , it is possible to fairly fit different values of Q , with one value of η . In the inset, on the other hand, the dependence of η on L_2 is provided (strong dependence of η on L_2).

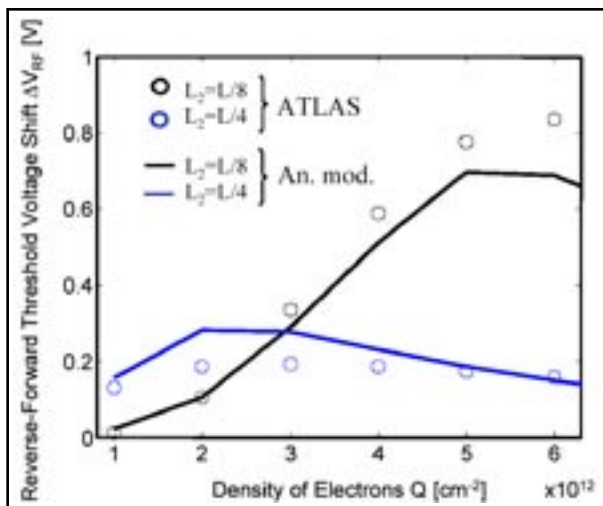


Figure 6. Reverse-forward threshold voltage shift ΔV_{RF} as a function of the density of electrons Q obtained from **ATLAS** results (circles) and the analytical model (solid line). Parameters are $L_2=L/8$ (35 nm) $\eta=3$ and $L_2=L/4$ (70 nm) $\eta=4$ (according to the inset of Figure 4(b)).

Already the plot of Figure 4(a) shows that the forward and reverse bits are not clearly detached for $L_2=L/4$ ($L_2=70 \text{ nm}$), and cannot be easily sensed as V_{th-F} and V_{th-R} are similar. From Figure 5, it is clear that *one-bit operation* appears for $L_2>70 \text{ nm}$ ($\Delta V_{RF} \approx 0V$). It is not required that the whole region of the channel is uniformly charged to have $V_{th-F} \approx V_{th-R}$.

Another interesting property is the charge density insensitivity of ΔV_{RF} , once a saturation limit is achieved.

In Figure 6 such a behavior is shown for $L_2=L/8$ ($L_2=35 \text{ nm}$) and for $L_2=L/4$ ($L_2=70 \text{ nm}$). In the case of $L_2=L/4$, for $Q>2 \times 10^{12} \text{ el./cm}^2$ the window between the forward and reverse threshold voltage is almost constant; while in the case of $L_2=L/8$, this property appears for $Q>5 \times 10^{12} \text{ el./cm}^2$. Therefore ΔV_{RF} can be used as an absolute indicator of the charged region dimension.

4. Comparison Between the Analytical Model and Experiments

Experiments performed on STMicroelectronics nanocrystal memory cells [4] confirm both the validity of the analytical model and suggest how to perform a reading procedure which allows to enhance the asymmetry between forward and reverse read.

From Figure 7, it is clear that raising V_{ds} enhances the electrostatic effect of trapped electrons, and decreases V_{th-F} to the value of the fresh cell threshold voltage, $V_{th-fresh}$. In experiments the maximum reading V_{ds} has been put at 1.5V. In Figure 8, the viability of this analytical model with different bulk voltages, V_b has been tested. The most relevant conclusion of this work is presented in

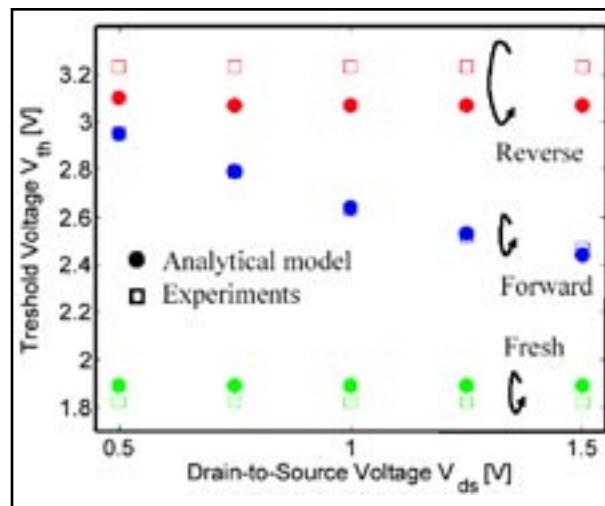


Figure 7. Analytical model vs data obtained from nanocrystal memories as a function of drain-to-source V_{ds} reading voltage.

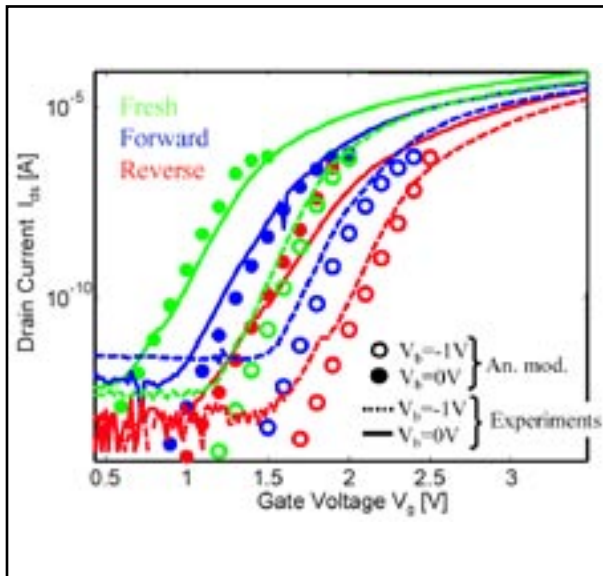


Figure 8. Analytical model versus experiments obtained from nanocrystal memories with $V_{ds}=1.5V$ and different bias condition for V_b .

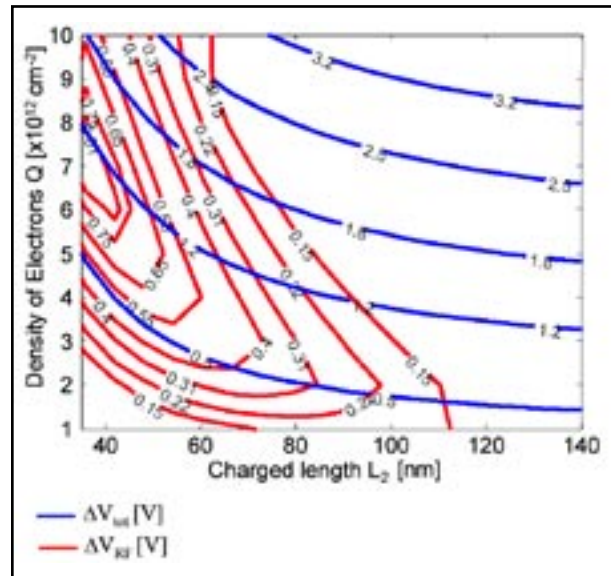


Figure 9. Contour plots of ΔV_{tot} and ΔV_{RF} as a function of the effective charged region L_2 and the charge density Q . Parameters are: $L=0.28\mu m$, $W=0.16\mu m$, $t_{ox}=15.5nm$, $V_{ds}=1.5V$, $V_b=-1V$. From the experimental data, we find the cross point between ΔV_{tot} and ΔV_{RF} values, and we deduce L_2 and Q .

Figure 9. As an example it is shown a contour plot of $\Delta V_{tot}(L_2, Q)$ and $\Delta V_{RF}(L_2, Q)$ that can be calculated from this model. From the two experimental parameters ΔV_{tot} (blue line) and ΔV_{RF} (red line) it is possible to find in the contour plot the crossing point and then deduce the values of L_2 and the density of electrons Q injected in the trapping medium.

5. Conclusions

A detailed model concerning Channel Hot Electron (CHE) electrostatic impact on forward/reverse reading has been provided. Both numerical simulations and experiments on nanocrystal memories, performed under different bias conditions confirm the viability of the model. At our knowledge, for the first time in literature, a contour plot is provided (Figure 9) where, from the experimental results at hand (ΔV_{tot} and ΔV_{RF}), it is possible to assess the effective charged length, L_2 and the density of injected electrons, Q . Support from EU projects ADAMANT (IST-2001-34234), SINANO (IST-506844) and from the CNR through the FIRB project is gratefully acknowledged.

References

- [1] B. Eitan, IEEE El. Dev. Lett., 21, 11, Nov. 2000.
- [2] E. Lusk, IEEE El. Dev. Lett., 22, 11, Nov. 2001.
- [3] I. Bloom, Microel. Eng., 59, 2001, 213-223.
- [4] B. DeSalvo, Proc. of IEDM 2003.
- [5] B. Muralidhar, Proc. of IEDM 2003.
- [6] L. Larcher, IEEE Trans. El. Dev., 49, 11, Nov. 2002.
- [7] Z. H. Liu, IEEE Trans. El. Dev., 40, 1, Jan. 1993.
- [8] Y. Taur, "Fundamentals of Modern VLSI Devices", CUP, 1998.

A New Efficient Quantum Method: The Bohm Quantum Potential Model

This article presents a new approach to model the quantum confinement of carriers in MOSFET or heterostructure. SILVACO has already included in its device simulator *ATLAS*, a Schrödinger-Poisson solver and Density-Gradient model. The Schrödinger-Poisson (SP) solver is the most accurate approach to calculate the quantum confinement in semiconductor but it cannot predict the currents flowing in the device. To overcome this limitation, *ATLAS* provides a Density Gradient (DG) model [1]. It allows the user to predict both the quantum confinement and the drift-diffusion currents along with the Fermi-Dirac statistics for a 2D structure. However this model exhibits poor convergence in 3D and with the hydrodynamic transport. Therefore, in collaboration with the University of Pisa, SILVACO has introduced in *ATLAS*, a new approach called Effective Bohm Quantum Potential (BQP) model. This model presented at SISPAD 2004 conference [2] exhibits many advantages. It includes two fitting parameters which ensure a good calibration for silicon or non-silicon materials, planar or non-planar devices. It is numerically stable and robust, and independent of the transport models used. Therefore it has been successfully implemented and tested in *ATLAS*. The table below summarizes the different models available in *ATLAS* related to the dimensionality and the transport models.

	1D	2D			3D		
		DD	EB	NEB	DD	EB	NEB
S-P	X						
DG	X	X			X		
BQP	X	X	X	X	X	X	X

X: available

S-P: Schrödinger-Poisson DD: drift-diffusion
 DG: Density Gradient EB: energy balance
 BQP: Bohm Quantum Potential NEB: non-isothermal energy balance

Historically, the definition of an effective quantum potential is Bohm's interpretation of quantum mechanics [3], and has generated other more recent derivations based on a first order expansion of the Wigner equation [4], or on the so-called density gradient approach [5]. The BQP model has a few advantages: it does not depend on the transport model (drift-diffusion or hydrodynamic); Fermi-Dirac statistics can be straightforwardly included; it provides two parameters for calibration, whereas the Density Gradient has only one fitting parameter; finally, it exhibits very stable convergence properties.

The definition of the effective quantum potential Q_{eff} is derived from a weighted average of the Bohm quantum potentials seen by all single particle wavefunctions, that can be expressed as:

$$Q_{eff} = -\frac{\hbar^2}{2} \gamma \frac{\bar{\nabla} \left[M^{-1} \bar{\nabla} (\psi^{\sigma}) \right]}{n^{\sigma}} \quad (1)$$

where M represents the effective mass tensor, n is the electron density per unit volume, ψ and ψ^{σ} depend on the eigen-functions of the confined system, and the operator $\bar{\nabla}$, which reduces to ∇ at equilibrium, allows to treat non-equilibrium problem and has been defined as:

$$\bar{\nabla} = \sum_i f_i \nabla (R_i^2) \quad (2)$$

where f_i is the occupation factor for the i -th state and R_i is the modulus of the i -th single particle wavefunction. The main advantage of these expressions is that the effective quantum potential does not depend on the transport model and, in the case of Fermi-Dirac distribution, can be discretized on a Delauney mesh as:

$$Q_{eff}(r_l) R_l = \frac{\hbar^2}{2} \gamma \sum_j \frac{\sigma_j}{d_{lj}} m_{ij}^{-1} \times \left[1 - \frac{N_c(r_l)}{N_c(r_j)} \left(1 + \frac{F_{\pm 1/2}(r_j) E_c(r_j) + Q_{eff}(r_j) - E_c(r_j) - Q_{eff}(r_j)}{k_B T(r_j)} \right) \right]^{\sigma_j} \quad (3)$$

where r_l is the position of the l -th point of the mesh, d_{lj} is the distance between a point r_l and r_j , A_{lj} is the area of the face of the Voronoi cell separating point l and j . Moreover, m_{ij} represents the effective mass tensor, $N_c(r)$ is the 3D density of states and $F_{\pm 1/2}$ represents the Fermi-Dirac integral of order $\pm 1/2$.

We have treated γ and σ_j in Equation (3), as fitting parameters avoiding to solve the solution of the Schrödinger equation. With two fitting parameters, instead of one like in DG model, the BQP model allows an additional degree of freedom for calibration.

Below are presented the results of simulations performed on simple structures of general interest in order to understand and verify the accuracy of the proposed model. The first device is a MOS-capacitor, a device in which the quantum confinement of electrons is predominant along one direction. The MOS-C has a 2 nm oxide thickness, a p-type concentration in the bulk $N_A = 10^{18} \text{ cm}^{-3}$, and a metal gate. In Figures 1, 2 and 3, we show the electron density profiles for different applied gate voltages and the C-V curve obtained with the two different methods (SP and BQP). For the BQP model, the best values for the fitting parameters are $\gamma = 0.46$ and $\sigma_j = 1.11$.

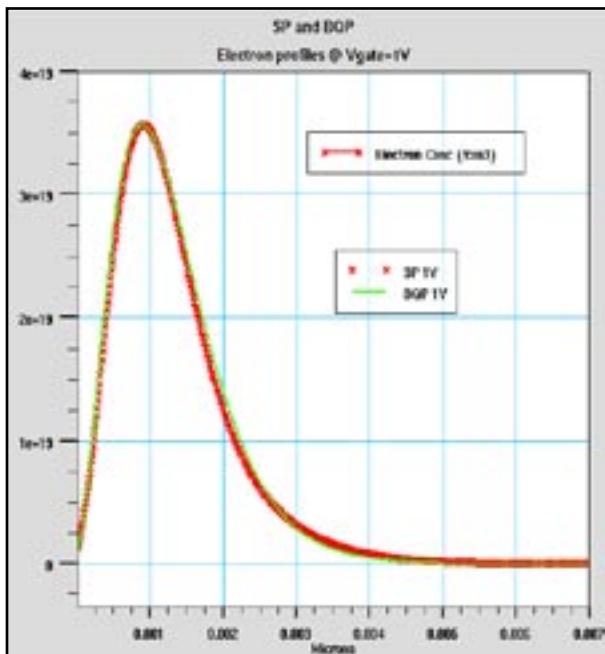


Figure 1. Electron density below the gate for a voltage applied to the gate of $V_g = 1$ V obtained with the BQP model and with the SP approach.

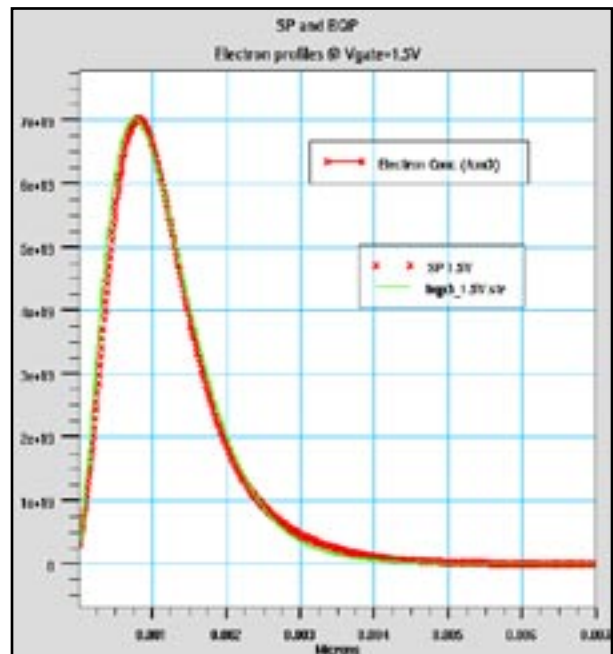


Figure 2. Same as figure 1 for $V_g = 1.5$ V.

As can be observed in Figures 1 and 2, the BQP method gives accurate height and shape of the carrier density profile as the applied voltage is varied. The method is also capable to well reproduce the carrier density per unit area obtained with the SP approach as shown in Figure 3.

The second device, in which electrons are confined in a quasi-one dimensional wire, is a FinFET depicted in Figure 4. The oxide thickness is 3 nm and the acceptor concentration is $N_A = 10^{18} \text{ cm}^{-3}$. Quantum confinement of electrons is strong both in x and y direction as shown with the isosurface of 10^{19} cm^{-3} in Figure 5 (for $V_{\text{drain}} = 0.1$ V and $V_{\text{gate}} = 1.15$ V).

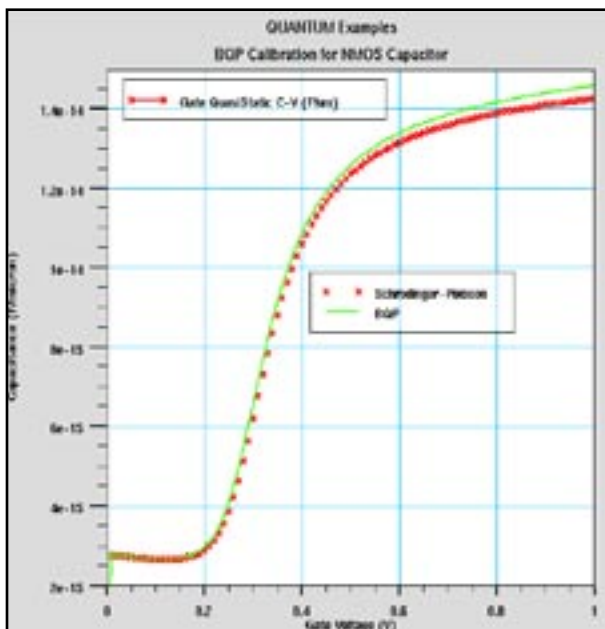


Figure 3. C-V curve obtained with the BQP model and SP approach.

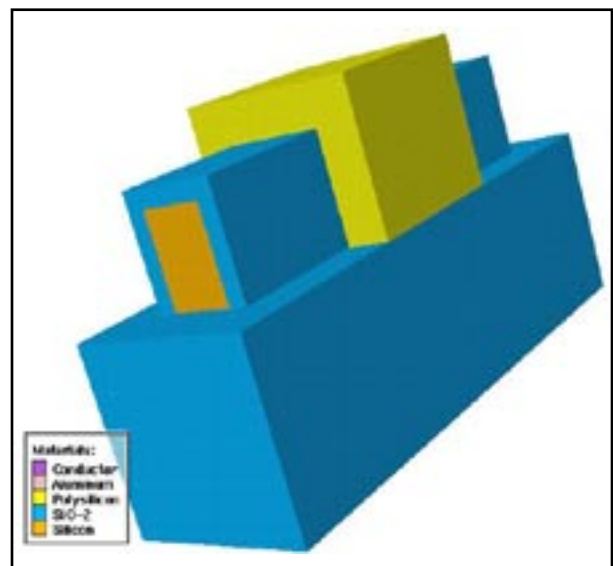


Figure 4. Representation of the FinFET composed by a silicon fin embedded in a SiO_2 layer. Also shown is the polysilicon gate deposited on the structure (source and drain electrodes are hidden for a better lisibility)

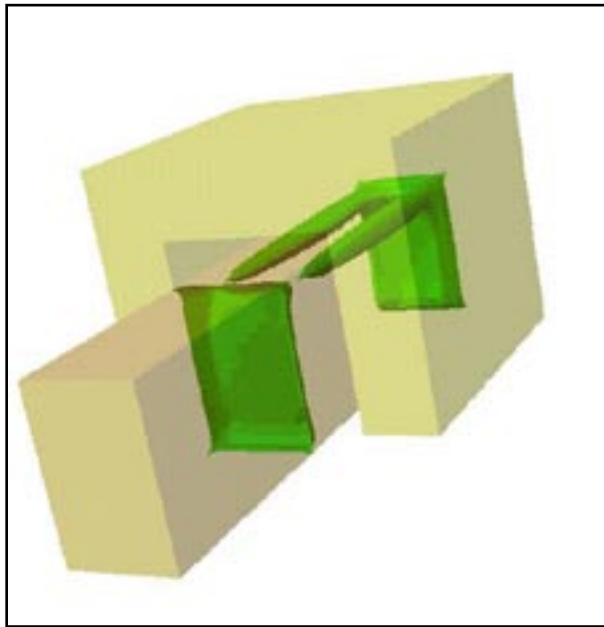


Figure 5. Representation of the 10^{19} cm^{-3} electron concentration isosurface inside the silicon fin.

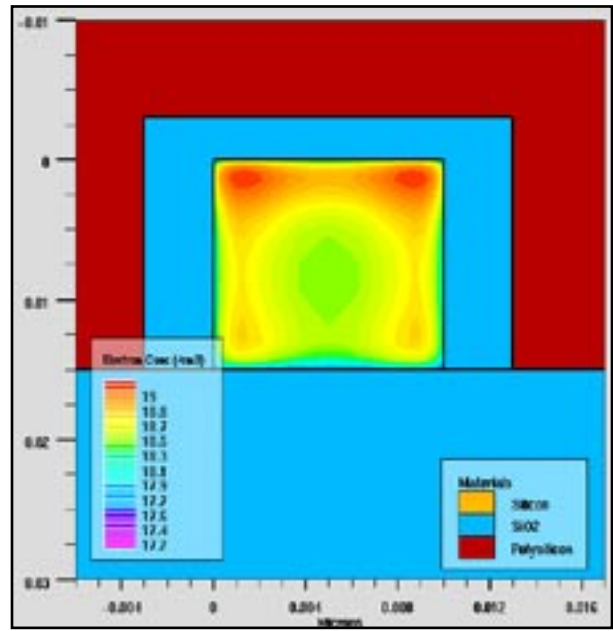


Figure 6. 2D cross-section made in the middle of the finFET of Figure 5. Electron concentration is shown.

Figures 5 and 6 show clearly the confinement of electrons under the gate oxide in the top corners of the silicon fin.

In conclusion, *ATLAS* proposed a new approach for quantum correction with the BQP model. The model is available both for drift-diffusion and energy transport models. With respect to previously published density gradient methods [1], the main advantages of this model are represented by the addition of one degree of freedom, which may provide better fit and improved calibration, by the possibility of including both Maxwell-Boltzmann and Fermi-Dirac statistics, and by its independence of the transport model adopted. SILVACO gratefully acknowledges support from University of Pisa.

References

- [1] A. Wettstein, A. Schenk, W. Fichtner, IEEE Trans. Electron Devices 48, 279 (2001).
- [2] G. Iannaccone, G. Curatola, G. Fiori, "Effective Bohm Quantum Potential for device simulators based on drift-diffusion and energy transport", SISPAD 2004
- [3] D. Bohm, Phys. Rev. 85, 166 (1952), 85, 180 (1952).
- [4] G. J. Iafrate, H. L. Grubin, and D. K. Ferry, J. Phys. C, 42, C10-307 (1981).
- [5] M. G. Ancona and G. J. Iafrate, Phys. Rev. B 39, 9536 (1989).

Simulating Selective and Non-Selective Epitaxy over Oxide Isolated Regions Using ATHENA

1.0 Introduction

In certain cases, most notably in modern bipolar and SiGe HBT structures, epitaxial steps are performed after the oxide isolation structures have been already created. Thus the initial surface prior to epitaxy may contain regions of crystalline silicon, polysilicon or insulators, usually silicon dioxide. In the case of LOCOS isolation, the surface is also non-planar. In such epitaxial cases, epitaxy can be divided into two general types:-

- (i) non selective epitaxy
- (ii) selective epitaxy

In the first case, silicon is deposited epitaxially onto any exposed crystalline surface, and polysilicon is deposited onto amorphous regions such as oxide isolation or regions where poly-silicon already exists.

In the second case, the use of selective chemistry increases the silicon layer seeding time on non crystalline surfaces to such an extent, that effectively silicon is only deposited epitaxially onto exposed crystalline surfaces. No polysilicon or amorphous silicon is deposited onto the oxide isolated regions.

In this article, the methodology for simulating both these scenarios is described.

2.0 Non Planar LOCOS Structure Example

In order to demonstrate the epitaxial capabilities, a standard LOCOS structure is used as the starting substrate, since this presents a surface that is both non planar and contains a combination of crystalline and non crystalline surfaces.

The structure prior to epitaxy is a simple LOCOS isolated active region as shown in Figure 1. Following a high temperature anneal to remove the native oxide, a typical ATHENA epitaxy statement would then be as follows:-

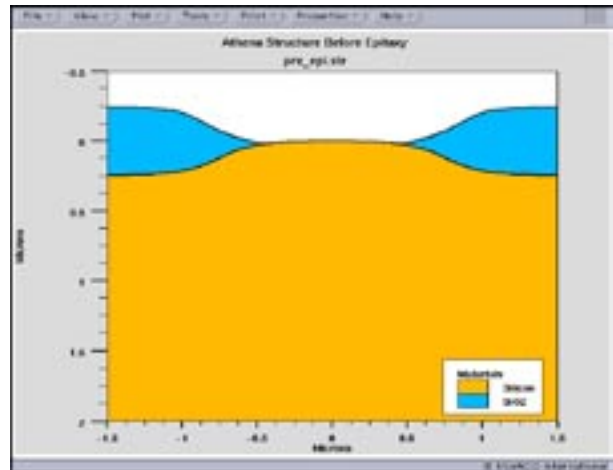


Figure 1 Structure Prior to Epitaxial Growth.

```
epitaxy time=1 temp=1000 thickness=0.2
divisions=8 c.boron=1e15 SI_TO_POLY
```

The key parameter in the ATHENA epitaxy statement that invokes the automated deposition of polysilicon on non crystalline regions of the device is "SI_TO_POLY". Other parameters such as c.boron=1e15 are simply inserted to emulate the un-intentional doping that occurs during epitaxy. Intentional doping can also be added using the same syntax format. After the Athena epitaxy statement above, the structure is now as shown in Figure 2.

Simulating selective epitaxy is now very simple because the epitaxial growth on the non crystalline regions is now polysilicon rather than silicon. Thus the simple statement

"etch poly all"

removes the poly silicon layer over the oxide leaving behind a structure as it would appear if selective epitaxy was used instead. After the etch above, the structure now appears as shown in Figure 3.

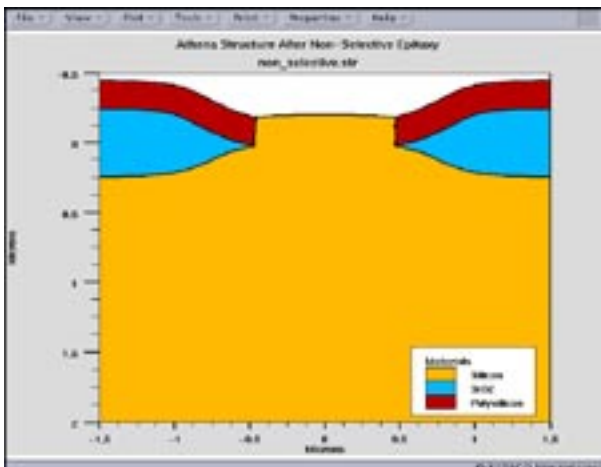


Figure 2 Structure After Non-Selective Epitaxial Growth.

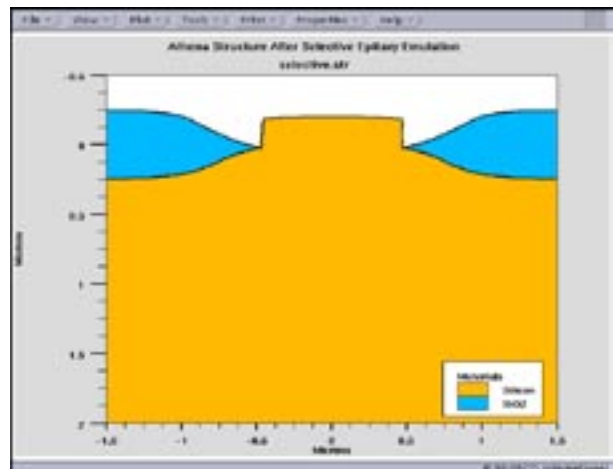


Figure 3 Structure After Emulating Selective Epitaxial Growth.

Calendar of Events

August

1	
2	
3	
4	
5	
6	
7	
8	
9	
10	
11	
12	
13	
14	
15	
16	
17	
18	
19	NSREC - Atlanta, GA
20	NSREC - Atlanta, GA
21	
22	
23	
24	
25	
26	
27	
28	
29	
30	

September

1	
2	SISPAD - Munich, Germany
3	SISPAD - Munich, Germany
4	SISPAD - Munich, Germany
5	
6	
7	
8	
9	
10	
11	
12	
13	
14	
15	
16	
17	
18	
19	
20	ESSDERC - Leuven, Belgium
21	ESSDERC - Leuven, Belgium
22	ESSDERC - Leuven, Belgium
23	ESSDERC - Leuven, Belgium
24	ESSDERC - Leuven, Belgium
25	
26	
27	
28	
29	
30	
31	

Bulletin Board



Silvaco at NSREC

The 2004 IEEE International Conference on Nuclear and Space Radiation Effects features papers describing nuclear and space radiation effects on electronic and photonic materials, devices, circuits, sensors, and systems, as well as semiconductor processing technology and techniques for producing radiation-tolerant (hardened) devices and integrated circuits.



SmartSpice-SEE

Silvaco's SEE Design Flow is an integrated solution to the severe reliability issues caused by Single Event Effects (SEE). *ATLAS 2/3D* SEE Module and *SmartSpice-SEE* provide the physics-based simulation at the device, circuit, and block level. Our SEE design flow connects device and circuit simulation results, full-chip parasitic extraction and fault simulation into a comprehensive solution to identify, analyze, and mitigate SEE

If you would like more information or to register for one of our workshops, please check our web site at <http://www.silvaco.com>

The Simulation Standard, circulation 18,000 Vol. 14, No. 11, August 2004 is copyrighted by Silvaco International. If you, or someone you know wants a subscription to this free publication, please call (408) 567-1000 (USA), (44) (1483) 401-800 (UK), (81)(45) 820-3000 (Japan), or your nearest Silvaco distributor.

The following trademarks and service marks are the property of Silvaco International. Registered Marks:® Virtual Wafer Fab, Silvaco. Trademarks:™ Simulation Standard, ATHENA, Analog Alliance, Legacy, Manufacturing Tools, Automation Tools, SFLM, VICTORY, Ranger3D Nomad, VYPER, SmartSpice, PSTATS, UTMOST IV, Measure, DISCOVERY, MERCURY, Optolith, TCAD Driven CAD, TonyPlot3D, RESILIENCE, Flash, ATHENA Interpreter, Interactive Tools, DeckBuild, DevEdit, ANALOG EXPRESS, CELEBRITY, SSuprem3, ATLAS, ATLAS Interpreter, Luminous2D/3D, MC Implant, S-Pisces, TonyPlot, FastLargeSignal, SmartStats, Ferro, DevEdit3D, Interpreter, Quantum2D/3D, SDDL, Circuit Optimizer, MaskViews, TFT2D/3D, Radiant, SSuprem4, Elite, FastBlaze, Mocasim, Silicides, MC Depo/Etch, FastNoise, Clarity, Blaze/Blaze3D, Device3D, Frontier, TwinSim, MixedMode2D/3D, VCSELS, Maverick, Envoy, Giga2D/3D, FastGiga, Guardian, Scout, FastMixedMode, Laser, Dragon, Expert, Spirit, Beacon, Savage, Harm, Zenith, Vision, Scholar, SN, UTMOST, UTMOST II, UTMOST III, UTMOST IV, PROMOST, SPAYN, ExpertViews, UTMOST IV Fit, FastSpice, Twister, Blast, MixSim, SmartLib, TestChip, Promost-Rel, RelStats, RelLib, Ranger, LISA, QUEST, EXACT, CLEVER, STELLAR, HIPEX-RCR, HIPEX-Net, HIPEX-RC, Connecting TCAD to Tapeout, and UTMOST IV Spice Modeling. All other product or company names are trademarks of their respective owners.

Hints, Tips and Solutions

Robin Jones Ph.D., Senior Applications and Support Engineer

The subject of how to use the EXTRACT statement in *DeckBuild* often arises. The EXTRACT statement is a very useful tool for analysing data and can be performed on both structure and log files.

As means of explanation let us consider an EXTRACT statement performed on a log file.

The EXTRACT statement by default will work on the current log file in a simulation.

Looking at a full EXTRACT syntax statement we have:

```
extract name="max. gate-source  
cap. Vgs=0 " max(curve(frequency,  
C."Gate""Source"))
```

The EXTRACT statement must first create its own curve to work on, in the above syntax we therefore have `curve(frequency, C."Gate""Source")`. This essentially goes to the current log file and creates a curve of frequency versus gate-source capacitance.

The keyword `max` is then used to pick the maximum value on the curve, this value then gets assigned to the variable `"max. gate-source cap. Vgs=0 "`.

It is often very useful for validation purposes for the user to output the curve created by the EXTRACT command. This is easily performed by adding an additional extract statement with an outfile command added to it, e.g. `extract curve(frequency, C."Gate""Source") outfile="testa_extract.dat"`

Figures 1(a) and (b) demonstrates this technique, Figure 1(a) shows the actual log file that the EXTRACT statement is working on, figure 1(b) shows the curve that the EXTRACT statement has produced.

Both EXTRACT statements would appear in the input deck as:

```
extract curve(frequency, C."Gate""Source")  
outfile="testa_extract.dat"  
extract name="max. gate-source cap. Vgs=0 "  
" max(curve(frequency, C."Gate""Source"))
```

What if you want to perform an EXTRACT on a previous log file, can you do this?

In order to do this you just add another extract statement with the keyword `init infile=""`, e.g.

```
extract init infile="hemtex06_ac.log"
```

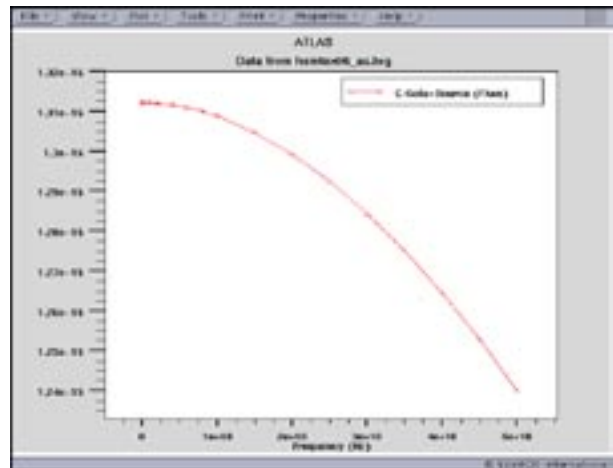


Figure 1a.

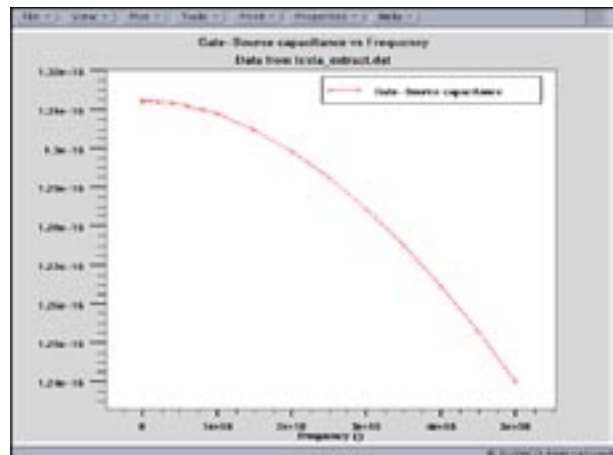


Figure 1b.

The three statements discussed above would appear as:

```
extract init infile="hemtex06_ac.log"  
extract curve(frequency,  
C."Gate""Source") outfile="testa_  
extract.dat"  
extract name="max. gate-source  
cap. Vgs=0 " max(curve(frequency,  
C."Gate""Source"))
```

Call for Questions

If you have hints, tips, solutions or questions to contribute, please contact our Applications and Support Department
Phone: (408) 567-1000 Fax: (408) 496-6080
e-mail: support@silvaco.com

Hints, Tips and Solutions Archive

Check out our Web Page to see more details of this example plus an archive of previous Hints, Tips, and Solutions
www.silvaco.com

Join the Winning TCAD Team!

- PROCESS AND DEVICE APPLICATION ENGINEERS
- SPICE APPLICATIONS ENGINEERES
- CAD APPLICATIONS ENGINEERES
- SOFTWARE DEVELOPERS

EMAIL TO: CAREERS@SILVACO.COM



SILVACO

INTERNATIONAL

USA Headquarters:

Silvaco International

4701 Patrick Henry Drive, Bldg. 2
Santa Clara, CA 95054 USA

Phone: 408-567-1000

Fax: 408-496-6080

sales@silvaco.com

www.silvaco.com

Contacts:

Silvaco Japan

jpsales@silvaco.com

Silvaco Korea

krsales@silvaco.com

Silvaco Taiwan

twsales@silvaco.com

Silvaco Singapore

sgsales@silvaco.com

Silvaco UK

uksales@silvaco.com

Silvaco France

frsales@silvaco.com

Silvaco Germany

desales@silvaco.com

*Products Licensed through Silvaco or e*ECAD*

